Pharmaceutical Research, Vol. 25, No. 2, February 2008 (© 2007)
DOI: 10.1007/s11095-007-9477-z

Research Paper

Velocity Distribution and Shear Rate Variability Resulting from Changes in the Impeller Location in the USP Dissolution Testing Apparatus II

Ge Bai[1] and Piero M. Armenante[1,2]

Received July 2, 2007; accepted October 11, 2007; published online November 27, 2007

Purpose. The United States Pharmacopoeia (USP) imposes strict requirements on the geometry and operating conditions of the USP Dissolution Testing Apparatus II. A previously validated Computational Fluid Dynamics (CFD) approach was used here to study the hydrodynamics of USP Apparatus II when the impeller was placed at four different locations, all within the limits specified by USP.
Method. CFD was used to predict the velocity profiles, energy dissipation rates, and strain rates when the impeller was placed in the reference location (centrally mounted, 25 mm off the vessel bottom), 2 mm off-center, 2 mm higher, and 2 mm lower than the reference location.
Results. Small changes in impeller location, especially if associated with loss of symmetry, produced extensive changes in velocity profiles and shear rates. Centrally located impellers, irrespective of their off-bottom clearance, produced non-uniform but nearly symmetric strain rates. The off-center impeller produced a more uniform but slightly asymmetric strain rate distribution.
Conclusions. The system hydrodynamics depends strongly on small differences in equipment configurations and operating conditions, which are likely to affect significantly the flow field and shear rate experienced by the oral dosage form being tested, and hence the solid–liquid mass transfer and dissolution rate.

KEY WORDS: CFD; computational fluid dynamics; hydrodynamics; off-center impeller; USP dissolution testing apparatus.

INTRODUCTION

The USP Dissolution Testing Apparatus II is the most widely used of all the dissolution testing devices listed in the United States Pharmacopoeia (USP) (1). Although this apparatus has been in use since the USP first officially introduced it some 30 years ago (2) and despite the fact that it still is the most widely used dissolution testing apparatus in the pharmaceutical industry today, concerns remains about the apparatus susceptibility to significant error and test failures, as indicated by many literature reports (3–10).

Dissolution testing failures can have a significantly negative and costly impact on pharmaceutical companies (11–13). Even when USP calibrator tablets are used, errors and inconsistencies have been reported (4,6,9,14,15). Many of these same studies indicate that the system hydrodynamics could play a key role in the variability and the poor reproducibility of the testing results.

Only limited information is available in the literature on the hydrodynamics of the USP Dissolution Testing Apparatus II (referred to here as USP Apparatus II) and the effects of operating and geometric variables on the velocity distribution inside the apparatus, although this kind of information is critical to enhance our fundamental understanding on the intrinsic causes of the inconsistencies in test results. To date, only a few research groups have studied the hydrodynamics of USP Apparatus II systems (8,14–20). The approach used in these studies was (a) only experimental, using Laser-Doppler Velocimetry (LDV), Particle Image Velocimetry (PIV), or Planar Laser-Induced Fluorescence (PLIF), (b) only computational using Computational Fluid Dynamics (CFD), or (c) a combination of both. Those authors that used both approaches found that CFD can appropriately predict the hydrodynamic behavior of the system (14,15,18–20). In particular, recent work by our group has shown that CFD-based fluid flow predictions agree well with the tridimen-

[1] Otto H. York Department of Chemical Engineering, New Jersey Institute of Technology, 323 M. L. King Boulevard, Newark, New Jersey 07102-1982, USA.
[2] To whom correspondence should be addressed. (e-mail: piero.armenante@njit.edu)

NOTATION: D, Impeller diameter, m; D_{AB}, Diffusivity, $m^2\ s^{-1}$; k, Turbulence kinetic energy, $m^2 \cdot s^{-2}$; r, Radial coordinate measured from vessel centerline, m or mm; **S**, Rate-of-deformation tensor, s^{-1}; Sc, Schmidt number, $\mu\ (D_{AB} \cdot \rho)^{-1}$, dimensionless; S_{ij}, Component of the rate-of-deformation tensor, s^{-1}; T, Vessel diameter, m or mm; u, Velocity, m/s; u_{axial}, Axial component of the velocity, m/s; u_{radial}, Radial component of the velocity, m/s; $u_{tangential}$, Tangential component of the velocity, m/s; u_{tip}, Impeller tip velocity, m/s; x_i, x_j, Coordinates in the i and j directions.
GREEK SYMBOLS: γ, Magnitude of strain rate, s^{-1}; ε Turbulent energy dissipation rate, $m^2 \cdot s^{-3}$; μ Liquid viscosity, $kg \cdot m^{-1} \cdot s^{-1}$; ρ Liquid density, $kg \cdot m^{-3}$; ω Specific energy dissipation rate, s^{-1}; τ Stress tensor, kg m^{-1} s^{-2}; φ Angle between vessel vertical centerline and line through location of interest on vessel bottom and center of vessel bottom hemisphere, degrees

sional LDV measurements of the velocity profiles at different locations within the USP Apparatus II (19) and can also be used to appropriately predict flow-dependent phenomena, such as blend time (20). These authors have shown that under the standard operating conditions and geometry prescribed in the USP (i.e., centrally located impeller placed 25 mm off the vessel bottom and rotating at 50 rpm in 900 mL of fluid) the flow in the bottom region of the USP Apparatus II vessel, where the dissolving tablet resides, is weak but very complex. In the region just below the impeller, the velocity magnitude is extremely low, but the fluid velocity changes significantly in intensity and direction across short distances. These results imply that the exact location of the dissolving tablet and, possibly, minor variations in the impeller position with respect to the tablet and/or the vessel may introduce significant variations in the flow and the strain experienced by the tablet, which, in turn can affect the dissolution process and the dissolution profile.

In this work, the effect of the location of the impeller relative to the vessel on the velocity profiles in the USP Apparatus II was studied, with special attention being paid to the velocity distribution and shear rates near the vessel bottom. The impeller position can differ from the standard location prescribed by the USP as a result of operator's error

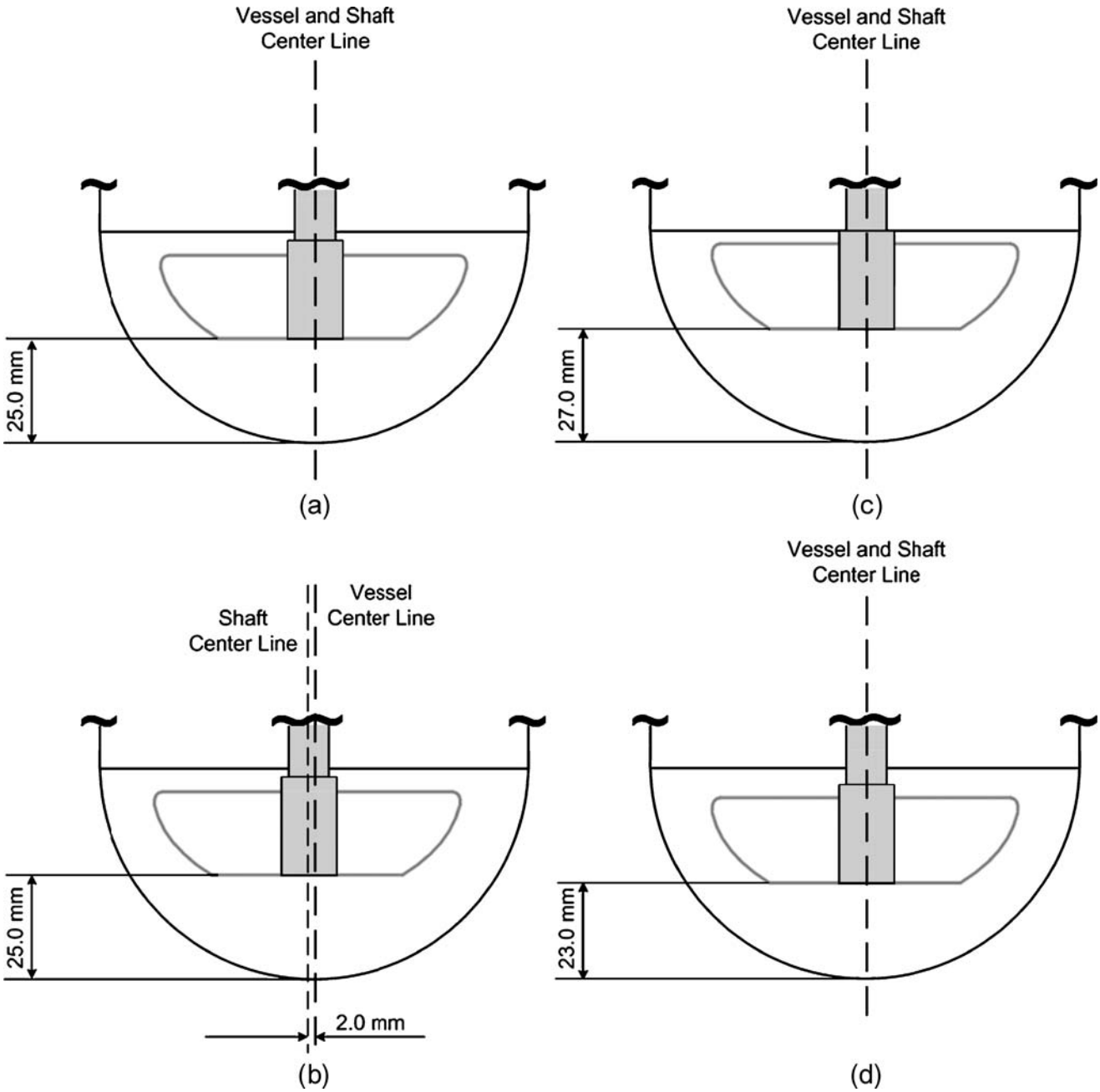

Fig. 1. Impeller location in the four impeller-vessel configurations studied in this work: **a** standard impeller location (centered; 25 mm off-bottom clearance); **b** off-centered (2 mm off-center; 25 mm clearance); **c** higher location (centered; 27 mm off-bottom clearance); and **d** lower location (centered, 23 mm off-bottom clearance).

(e.g., incorrect off-bottom impeller location, misalignment of vessel), equipment problem (e.g., slightly bent impeller shaft), or simply by operating within the tolerances described in the USP for positioning the impeller. According to the USP (1), the impeller off-bottom clearance should be 25 mm±2 mm, while the impeller shaft can be positioned 2 mm off center and still meet the test requirements. The basic hypothesis of this work was that given the previously reported extreme changes in velocity magnitude and direction with position near the vessel bottom, even for the standard impeller location, placing the impeller in such diverse locations would result in different flow patterns. To the best of our knowledge, this issue has received no attention to date.

Therefore, the specific objective of this study is to quantify the changes in velocity profiles, energy dissipation, and strain rate distribution in a USP Apparatus II when the impeller is placed at the following four locations in the vessels (corresponding to the four cases examined here), as shown in Fig. 1: (a) standard impeller location (centered; 25 mm off-bottom clearance); (b) off-centered (2 mm off-center; 25 mm clearance); (c) higher location (centered; 27 mm off-bottom clearance); and (d) lower location (centered, 23 mm off-bottom clearance). All four impeller locations are within the USP specifications. The results of this work are based on CFD predictions that had been previously experimentally validated for the standard impeller location via LDV measurements (19).

NUMERICAL CFD METHOD

Predictions of the velocity distribution, turbulence levels, and strain rates inside the USP Apparatus II were obtained using a commercial pre-CFD mesh generator (Gambit 2.1.6) coupled with a CFD software package (Fluent 6.2.16). The full 360°-vessel geometries were incorporated in the simulations.

Mesh Generation and Mesh Quality

Figure 2 shows the basic geometry of the USP Apparatus II modeled in this work, consisting of an unbaffled, cylindrical, glass vessel with a hemispherical bottom, an internal diameter, T, of 100.16 mm, and a liquid volume of 900 mL. The exact geometry of each element of the impeller was obtained by measuring the dimensions of an experimental apparatus provided by researchers at Merck & Co., and is reported elsewhere (19). The impeller modeled here had a slightly enlarged diameter shaft at the blade, resembling a collar, as opposed to the uniform shaft diameter, including the portion at the blade, typical of the USP design. The radius of this collar was only 1.6 mm larger than that of the rest of the shaft (19), but the geometric differences between this system and the typical USP system are so minimal that the result obtained here are expected to be equally valid for the USP impeller with no collar.

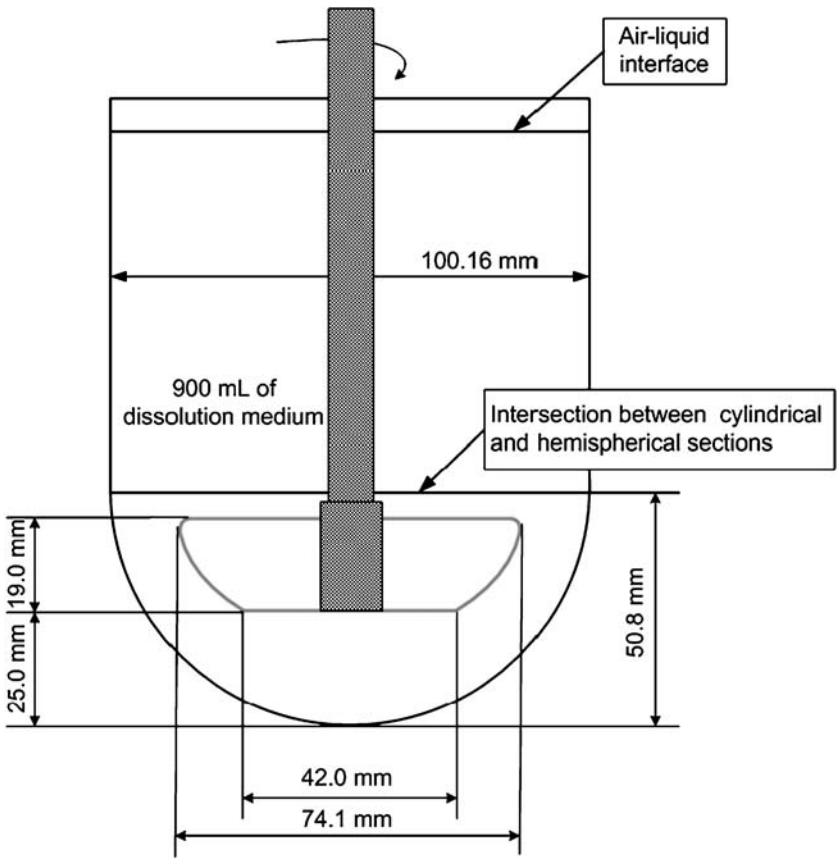

Fig. 2. Basic geometry of USP Dissolution Testing Apparatus II.

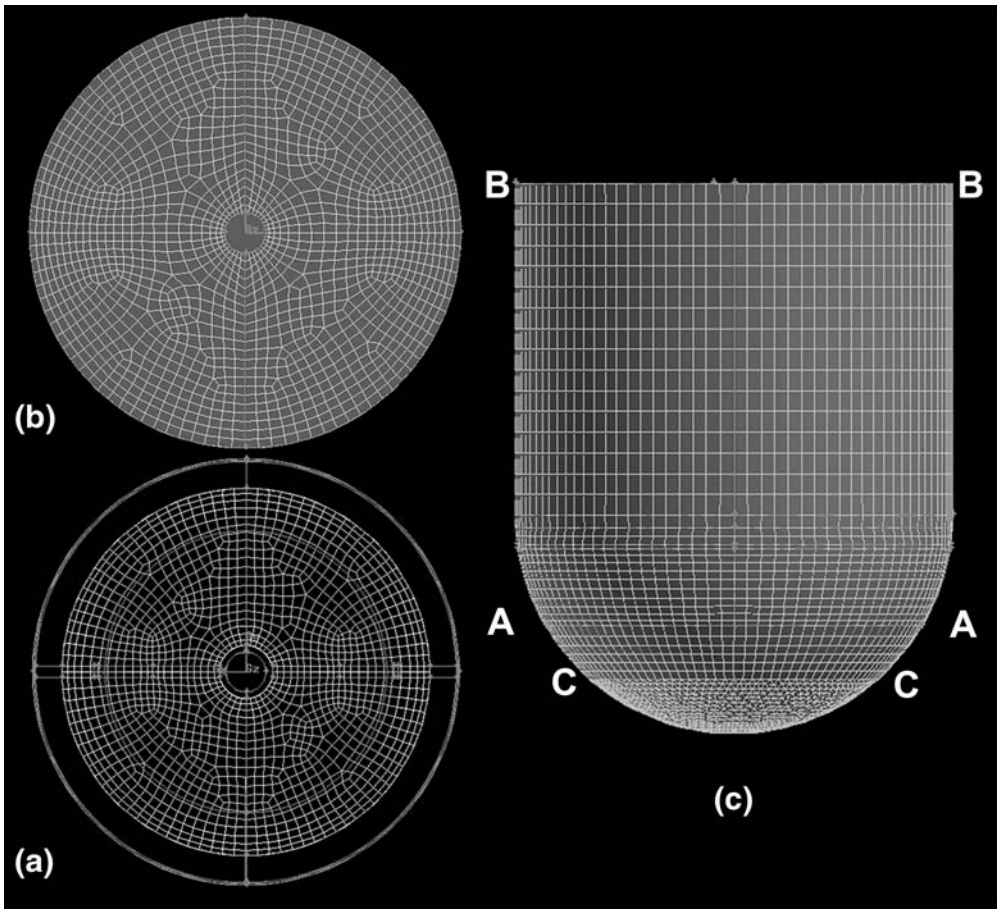

Fig. 3. Mesh used in the CFD simulation for the standard impeller location: **a** starting face on iso-surface at A–A; **b** top face on iso-surface at B–B; **c** axial, side view of mesh.

Four different meshes were generated to model the four cases examined here, each mesh corresponding to a different impeller location in the vessel. A hybrid mesh was initially generated for Case (a), in which the impeller is in the standard location (centrally located within the vessel with a 25 mm clearance): starting from a pre-meshed horizontal cross section (Fig. 3a) where the bottom edge of the impeller lies (section A–A in Fig. 3c), a structured Cooper-type hex mesh was generated by extending and projecting the face mesh up to the liquid-air surface (Fig. 3b, and section B–B in Fig. 3c) and down to a horizontal plane 12.35 mm below the lower edge of the impeller (section C-C in Fig. 3c). An unstructured, tetrahedral mesh was created in the lower bottom portion of the vessel. The overall mesh contained 80,262 cells, 219,590 faces, and 62,472 nodes. Significant attention was paid to construct a mesh that was of high quality for the subsequent CFD use (19). A similar approach was used to generate the meshes for Cases (c) and (d), the only difference being the location of the impeller.

For Case (b) in which the impeller was 2 mm off center, a Multiple Reference Frame (MRF) approach (21) was used for mesh generation and CFD simulation, since the domain was no longer symmetric. Accordingly, the vessel volume was divided in two domains: an inner cylindrical domain including the impeller and symmetric with respect to the impeller, and an outer domain comprising the region between the inner domain and the vessel wall. Meshes were generated in each domain following an approach similar to that used to generate the meshes for Cases (a), (c) and (d).

The meshes for all four cases contained similar number of cells.

Boundary Conditions and Reference Frames

In all four cases, the no-slip condition in the appropriate frame of reference was assumed at all solid surfaces. The air-water interface was always assumed to be flat (a reasonable assumption given the low agitation speed, as experimentally verified), and it was modeled as a frictionless surface, i.e., the normal gradients of all variables were zero at this interface.

A single reference frame approach was used in the CFD simulations for Cases (a), (c), and (d): the vessel wall was assumed to be rotating, and the impeller was stationary, although the appropriate body forces were included in the computation to account for the non-inertial characteristics of the rotating reference frame.

As for Case (b) in which the impeller was no longer in the center of the vessel and the MRF approach was used instead, the conservation equations in the inner domain frame were transformed into a rotating reference frame and the flow was computed in a steady state manner. The outer domain was modeled at steady state in a stationary reference frame. The results were transformed back to stationary reference frame at the end of the simulation.

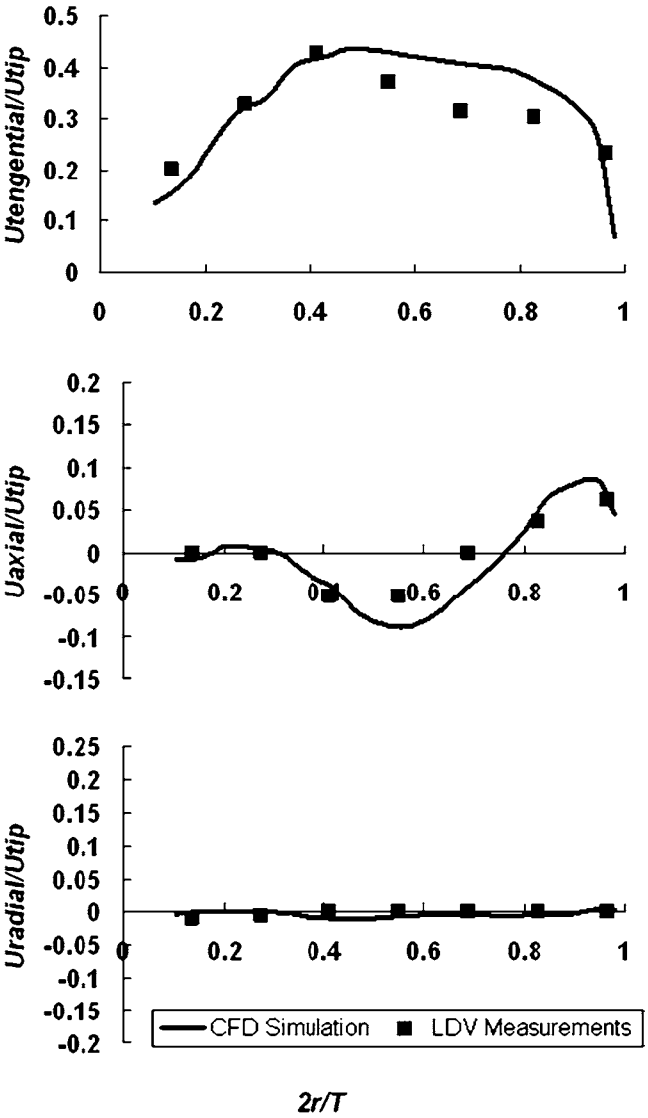

Fig. 4. Comparison between the LDV data of Bai *et al.* (19) and the CFD predictions for tangential velocity (*upper panel*), axial velocity (*middle panel*), and radial velocity (*lower panel*) on an iso-surface 50 mm above the intersection between the cylindrical section and the semi-spherical section of the USP Dissolution Testing Apparatus II vessel.

CFD Approach

The conservation equations for mass and momentum were solved by the CFD solver (Fluent 6.2.16) for each of the control volumes generated during the discretization process of the computational domain, based on the previously generated meshes. All simulations were carried out on a Dell Precision 650 Workstation, equipped with two Intel XEON 2.8 Gigahertz processors and 2 GB of random access memory (RAM). A typical simulation required some 40,000 iterations and about 30 h of CPU time to achieve conversion.

Based on the results of previous work, all simulations were conducted using as a turbulence model the k-ω model with low Reynolds number correction, which was selected here because its predictions matched more closely previously obtained experimental velocity data (19). Figure 4 shows a typical comparison between the LDV data of Bai *et al.* (19) and the CFD predictions for tangential, axial, and radial velocities on an iso-surface at 50 mm above the intersection between the cylindrical and the semi-spherical sections of the USP Apparatus II vessel.

RESULTS

Velocity Magnitude and Velocity Vectors

Figures 5 and 6 show the contours of the CFD-predicted velocity magnitude on a vertical cross section through the impeller shaft for two different orientations of the impeller and different impeller locations. The vertical plane where the impeller blades lie is defined here as the y-plane, and the plane perpendicular to y-plane is defined as the x-plane. Figure 7 presents the velocity vectors for different impeller locations on a horizontal cross section 43.75 mm below the horizontal plane where the cylindrical and horizontal sections of the vessel intersect. Figure 8 shows the velocity vectors on a vertical cross section containing the impeller blades. Finally, the plots in Figs. 9 and 10 show expanded views of the velocity vectors in the bottom region of the vessel on a vertical cross section through the impeller shaft at two different orientations of the impeller for different impeller locations.

Standard Impeller Location (Centered; 25-mm Off-bottom Clearance)

Panels (a) in Figs. 5 and 6 show that the flow field in the USP Apparatus II vessel is symmetrical when the impeller is in the standard location. The fluid around the impeller is strongly dominated by the impeller's rotating action (Fig. 7a). The magnitude of the velocity near the tip of the impeller blades approaches the impeller tip speed. However, the velocity magnitude decays rapidly away from the impeller blades, especially when moving away in the axial and radial direction. In most regions of the vessel, the velocity magnitudes are smaller than 50% of the impeller tip speed. The lowest velocity magnitudes, which are 5% of the impeller tip speed or less, appear in a region, some 10 mm wide, located between the bottom edge of the impeller and the center of the vessel bottom. Figure 8a shows that the impeller blades push the flow radially towards the vessel wall. The radial flow is converted mostly to axial flow (upward and downward) after it impinges on the vessel wall. However, the flow is only directed upwards near the top edge of the blade. The flow is oriented downwards anywhere else in the gap between the passing impeller blade and the vessel wall. Two recirculation loops are observed in the vertical cross section, one above and the other below the impeller. The recirculation loop above the impeller "closes" near the surface of the dissolution medium at a relative radial location ($2r/T$) of about 0.4. Figures 9a and 10a show that the vertical recirculation loop below the impeller cannot penetrate the inner core region located between the impeller and the vessel bottom. The flow in this region is extremely complex, but also very weak, with velocities in the vertical plane on the order of 5% of the tip speed. As the impeller rotates, the core region just under the impeller expands (Fig. 9a) and contracts (Fig. 10a). Small changes in position along the vessel bottom result in

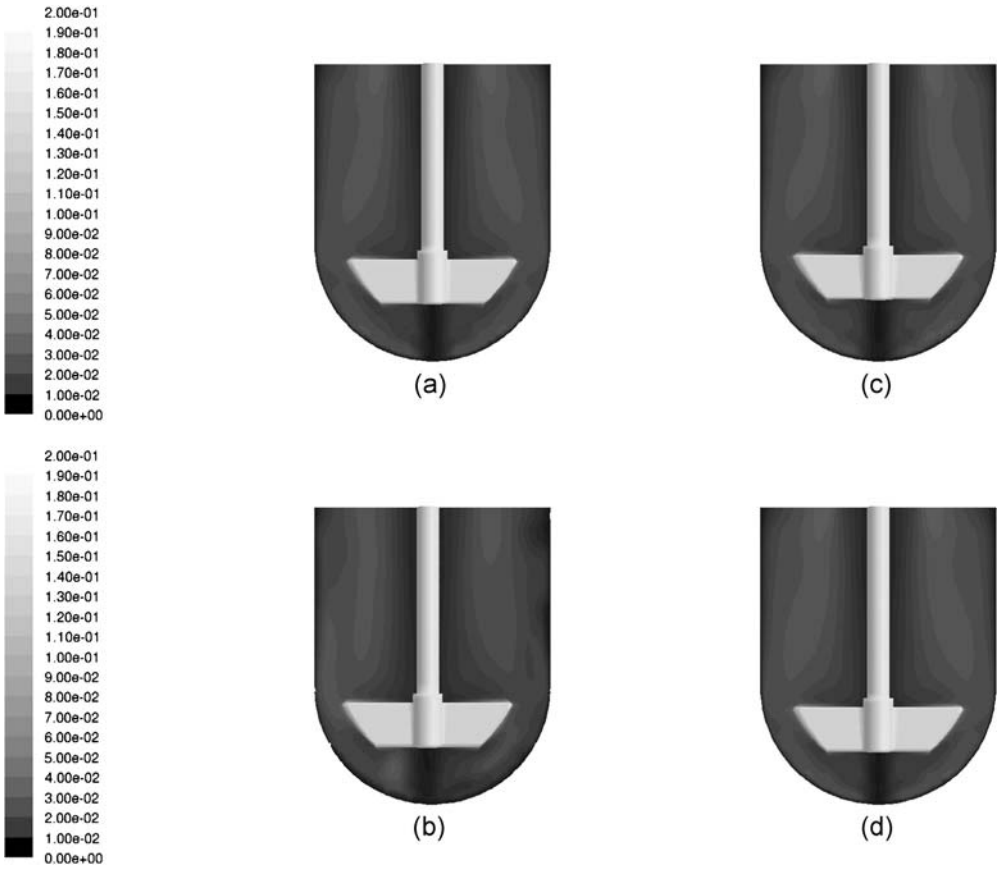

Fig. 5. Numerically predicted contours of the velocity magnitude (m/s) on the impeller plane (*y*-plane) for different locations of the impeller: **a** standard impeller location; **b** off-centered impeller location; **c** higher impeller location; **d** lower impeller location.

relatively large changes in both velocity magnitude and velocity direction. For example, by moving radially 2 to 5 mm in the plane of the impeller, the velocity near the bottom can vary from near zero to 1/3 of the tip speed.

Off-centered Impeller Location (2 mm Off-center, 25-mm Off-bottom Clearance)

Panels (b) in Figs. 5 and 6 present the contours of the velocity magnitude for the off-center impeller case. Although the impeller is displaced sideways by only a small distance (2 mm compared to a vessel radius of 50.08 mm, i.e., a 4% translation), the velocity magnitude plots show a significant non-symmetric distribution compared to the centrally placed case (Figs. 5a and 6a).

Figure 7b shows that even in the off-center case the tangential component of the velocity dominates over the other velocity components, although the tangential velocity is weaker compared to the standard case (Fig. 7a), especially in the region where the impeller-wall distance is larger. Compared to the corresponding standard case, the impeller asymmetry also produces higher axial and radial velocities in most regions of the vessel, especially on the side where the impeller-wall distance is smaller, both above and below the impeller. However, on the opposite side of the vessel, the regions where the velocity magnitude is very small (e.g., in upper region near the wall, and, more significantly, in the region below the impeller) actually expand, as indicated by the enlarged darker region, especially just under the impeller. Since the impeller rotates, the different regions rotate as well, thus exposing different portions of the vessel to highly fluctuating velocities and promoting mixing and recirculation.

The velocity vector plot (Fig. 8b) confirms these observations. Two recirculation loops can still be observed, above and below the impeller. However, the loops are no longer symmetric. As one can anticipate, on the side where the impeller blade is 2 mm closer to the vessel wall (the left side in the figure) the loops have higher velocity magnitude than at the same radial location on the opposite side.

Of special interest here are the plots for the region below the impeller (Figs. 9b and 10b). Since the impeller is off-center, the symmetric structure and the poorly mixed region below the shaft predicted for the standard case (Figs. 9a and 10a) are now largely removed. A stronger flow in the vertical plane now sweeps the entire lower region, creating alternating recirculation loops below both tips of the lower edge of the impeller. These loops move with the impellers, and the net result is that the entire vessel bottom region is affected. An eddy in the vertical plane can even be observed in Figs. 8b and 9b. It is also remarkable that the radially directed flow sweeping the central core region below the impeller now "feeds" a large upflow stream (shown on the left in the figures), which further promotes axial mixing within the vessel.

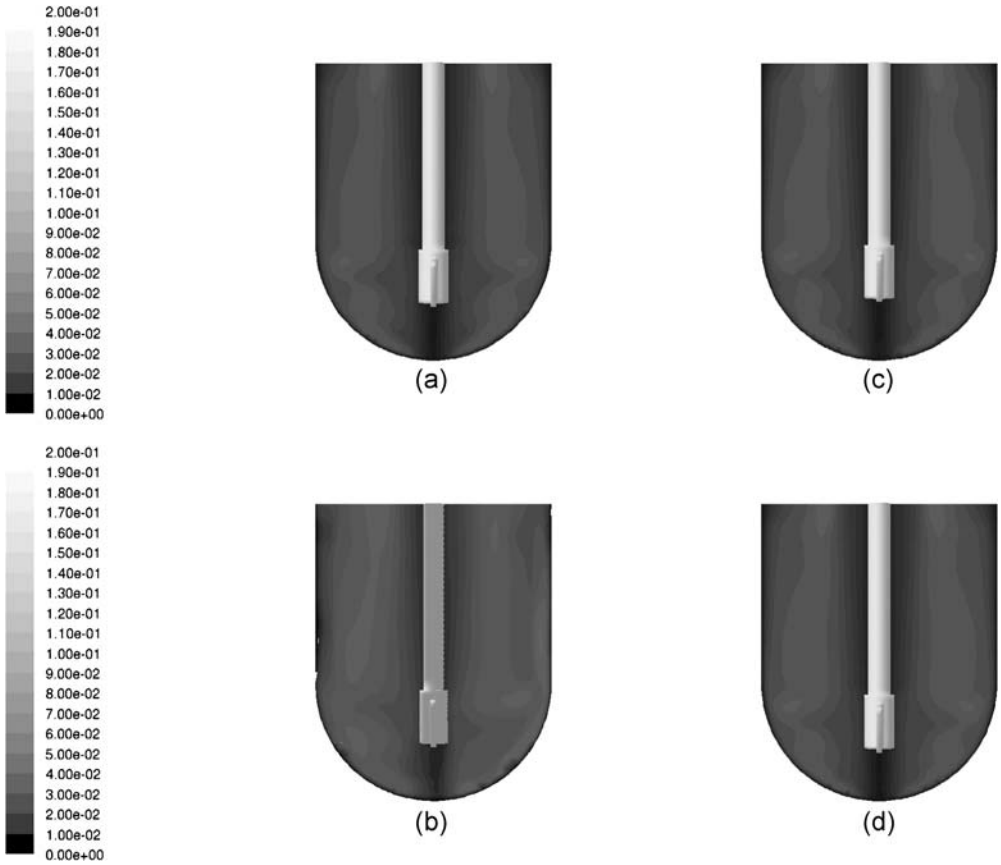

Fig. 6. Numerically predicted contours of the velocity magnitude (m/s) on the plane perpendicular to the impeller plane (*x*-plane) for different locations of the impeller: **a** standard impeller location; **b** off-centered impeller location; **c** higher impeller; **d** lower impeller location.

Higher Impeller Location (Centered; 27-mm Off-bottom Clearance)

Figures 5c and 6c show the contours of the velocity magnitude for the higher off-bottom clearance case. The differences in velocities between these figures and the corresponding figures for the standard impeller clearance are relatively small. The low velocity region below the impeller is larger for the higher impeller position simply because the impeller clearance is also larger. A slight increase in the velocity magnitude can be detected in the center near the vessel bottom.

The tangential component of the velocity does not appear to be appreciably affected by the increased off-bottom clearance (Fig. 7c) compared to the standard case (Fig. 7a), implying that the preservation of symmetry, and hence the resulting strong tangential flow, dominate over any other effects.

A comparison between the velocity vectors for the two cases (Fig. 8c *vs.* Fig. 8a), especially in the region below the impeller (Figs. 9c and 10c *vs.* Figs. 9a and 10a), shows that small velocity differences exist. For the higher impeller clearance case, the low velocity region below the impeller is characterized by slightly higher velocities in the axial and radial directions, and the region just around the low-mixing core region shows a stronger upward-directed flow. The probable cause for this effect is the larger gap between the impeller blades and the vessel wall, resulting in a slightly stronger pumping action by the impeller and a stronger flow in the lower recirculation loop (Fig. 9c and 10c). However, the difference in velocity profiles between the standard clearance case and the higher clearance case appears to be rather small.

In summary, although the higher impeller position places the impeller farther away from vessel bottom, the stronger pumping action produces a slightly stronger lower recirculation loop.

Lower Impeller Location (Centered; 23-mm Off-bottom Clearance)

Figures 5d and 6d show the contours of the velocity magnitude for the lower off-bottom clearance case. In general, the velocity magnitudes for this case are similar to those for the standard case. As in the higher impeller case, the tangential velocity is not significantly affected by the lower off-bottom clearance (Fig. 7d) compared to the standard case (Fig. 7a). Once again, symmetry prevails over other small effects.

A closer comparison of the velocity vectors for this case (Figs. 8d, 9d, and 10d) with those for the standard case shows that the differences are still small, but that the reduced volume of fluid below the impeller and the smaller gap, and hence the proximity of the fluid in this region to the impeller, promotes a slightly larger segregation of the fluid region just under the impeller from the other regions of the vessel. This

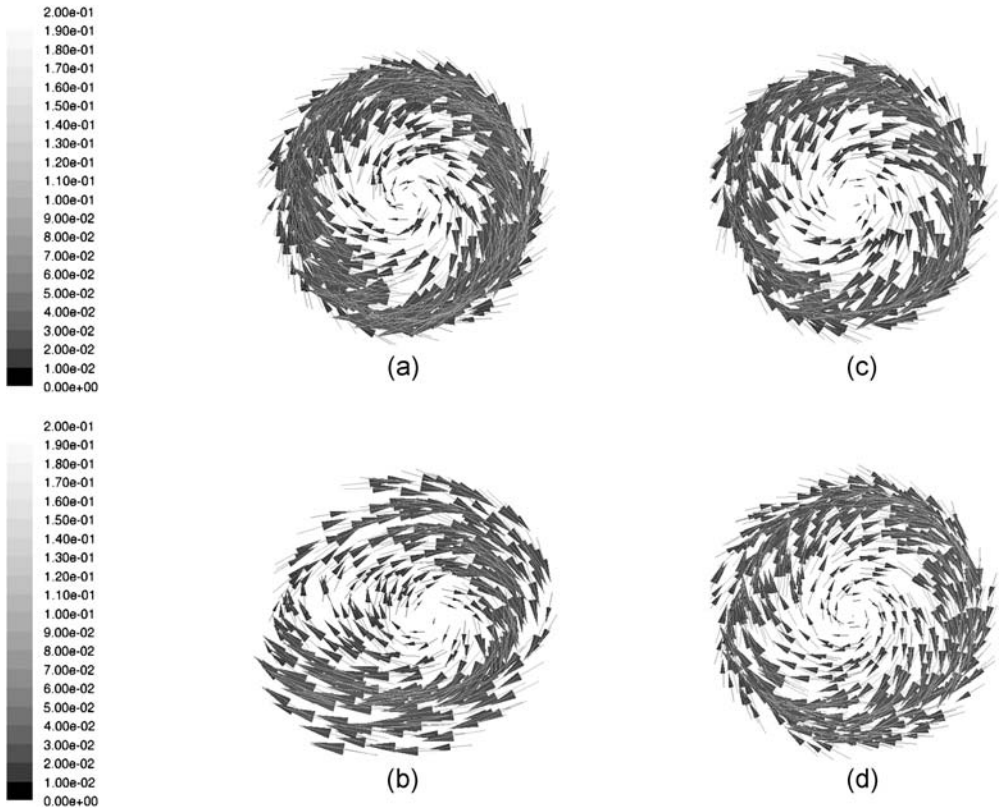

Fig. 7. Numerically predicted velocity vectors (m/s) on a horizontal plane below the impeller at $z=-43.75$ mm (where $z=0$ is the vertical plane at the intersection of the cylindrical and hemispherical regions of the vessel) for different locations of the impeller: **a** standard impeller location; **b** off-centered impeller location; **c** higher impeller location; **d** lower impeller location.

can be seen from the slightly expanded low velocity region just below the impeller shaft. In other terms, it becomes increasingly difficult for the fluid jet emerging radially from the blades to penetrate the central fluid core just below the impeller. This, in turn, slightly reduces the axial velocity component of the fluid just under the impeller and promotes segregation.

Energy Dissipation Rate

Figure 11 presents the distribution of the local CFD-predicted energy dissipation rates, ε (i.e., the rate of turbulence energy dissipation per unit mass), on the y-plane, for four different impeller locations. The energy dissipation rate is potentially relevant to dissolution process since in many equations for the mass transfer between suspended solids and the surrounding fluid the solid–liquid mass transfer coefficient k has been reported to be dependent on ε (22,23). Hence, the local value of the energy dissipation rate near the vessel bottom could affect the dissolution process if tablet fragments become suspended.

The CFD-predicted distributions of the energy dissipation rate in the USP Apparatus II are symmetric above and below the impeller in all cases except for the off-center impeller case (Fig. 11b). The highest energy dissipation rates were found around the impeller blades, near the wall in the impeller region, and near the vessel bottom. Whenever symmetry was present, ε dropped rapidly in the wall region just under the impeller shaft. However, if symmetry was lost, as in the off-center case, the energy dissipation rate was found to be more uniformly distributed below the impeller (Fig. 11b).

Strain Rate

The shear stress tensor, $\boldsymbol{\tau}$, is related to the rate-of-deformation tensor, $\mathbf{S}$, through the equation:

$$\tau = -\mu \mathbf{S} \tag{1}$$

where μ is the fluid viscosity. For an incompressible Newtonian fluid, the components of the rate-of-deformation tensor, S_{ij}, are given by (21,24):

$$S_{ij} = \frac{\partial u_i}{\partial x_j} + \frac{\partial u_j}{\partial x_i} \tag{2}$$

Then, the local value of magnitude of the strain rate (or simply "strain rate"), $\dot{\gamma}$, is defined as:

$$\dot{\gamma} = |\mathbf{S}| = \sqrt{\frac{1}{2}\sum_i \sum_j S_{ij}^2} \tag{3}$$

The strain rate represents the rate at which the velocity varies with distance when moving away from the point of interest. Since, based on boundary layer theory (21), the mass transfer boundary layer around a dissolving tablet can be

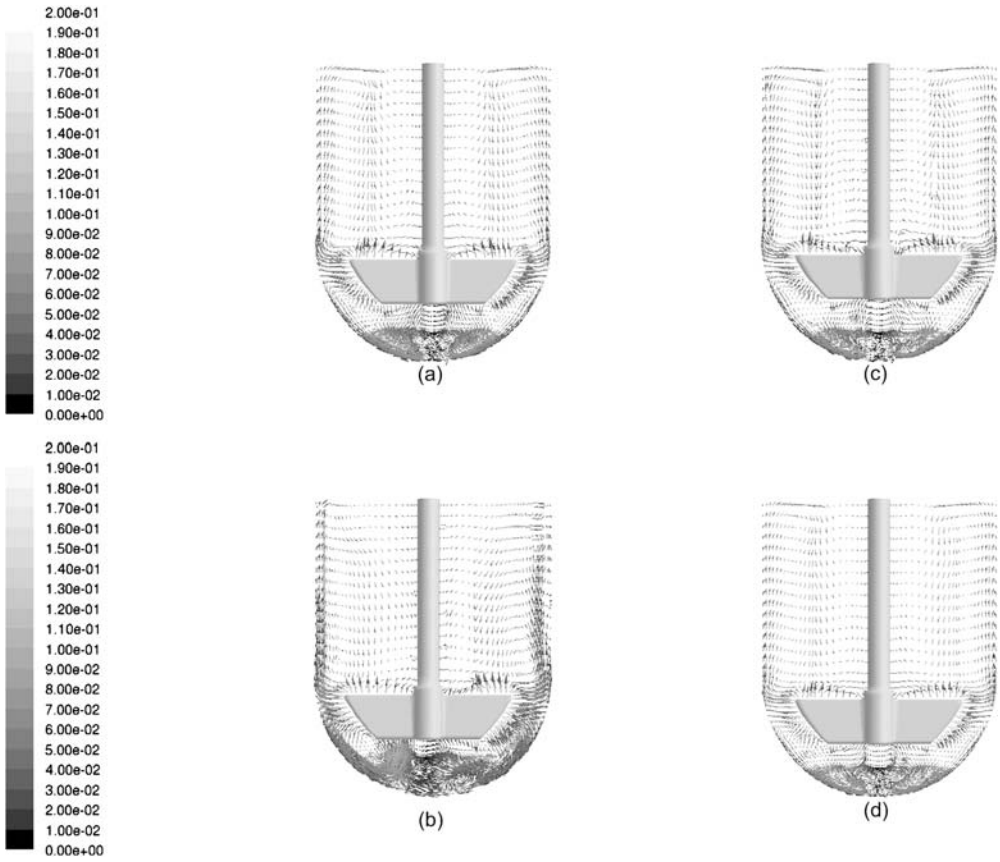

Fig. 8. Numerically predicted velocity vectors (m/s) on the impeller plane (*y*-plane) for different positions of the impeller: **a** standard impeller location; **b** off-centered impeller location; **c** higher impeller location; **d** lower impeller location.

assumed to be proportional to the velocity boundary layer (typically through $Sc^{1/3}$, where Sc is the Schmidt Number, $Sc = \mu/D_{AB} \cdot \rho$, information about the strain rate, i.e., knowledge of how rapidly the velocity changes when moving away from a surface (the vessel bottom in this case) can be very important in estimating the relative magnitude of the local mass transfer rates. High strain rate regions can be expected to experience higher mass transfer rates, and hence more rapid dissolution rates.

Figures 12 and 13 present the distribution of the local strain rate in the region below the impeller on the vertical plane of the impeller and on its perpendicular plane, respectively. The strain rate is generally higher next to the vessel wall, as one would expect. Panels (a), (c) and (d) in these figures, corresponding to the three cases in which the impeller is centrally located, show symmetrical strain rate distributions, all similar to each other. The impeller clearance does not appear to affect appreciably the strain rates, the only apparent difference being the size of the central low-strain region midway between the impeller and the vessel bottom. In the inner core (about 10 mm wide) just below the impeller shaft the strain rate drops significantly. This core is surrounded by a region of high wall strain rates. Hence, a rapid transition in strain rate occurs at the intersections between these two regions. The low-strain rate core region expands and contract with the blade passage as one can see by comparing corresponding panels (Panels (a), (c) and (d)) in Figs. 12 and 13.

The strain rate distribution is dramatically altered when the impeller is off-center (Figs. 12b and 13b). In this case, the strain rate along the vessel wall is more evenly distributed, and the central low-strain rate region at the wall is significantly reduced, in terms of both size and difference in strain rate magnitude with respect to the surrounding area. In addition, the location of the now reduced low-strain rate region moves with the impeller, as one can see by comparing Fig. 12b to Fig. 13b.

While Figs. 12 and 13 can be useful to visualize the strain rate distribution, Figs. 14 and 15 provide quantitative CFD-based predictions of the strain rates along the wall of the hemispherical portion of the vessel wall in the *y*-plain and *x*-plain, respectively. The abscissa in these figures is the angle φ, originating from the center of the sphere comprising the hemispherical vessel bottom, and measured starting from the vertical centerline to the point of interest, (i.e., $\varphi = 0°$ for the central point below the impeller, and $\varphi = \pm 90°$ for the points at the intersection between the hemispherical and cylindrical sections of the vessel). The raw strain rate predictions were very smooth in the domain mapped with the structured Cooper-type hex mesh. However, numerical scatter was observed at the interface between the structured upper mesh and the lower unstructured, tetrahedral mesh. Since this phenomenon occurred independently of where the partition between the two domains was located, a total of six points (three for $\varphi < 0°$ and three for $\varphi > 0°$) located at the domain interface, were discarded out of some 150. Some scattering

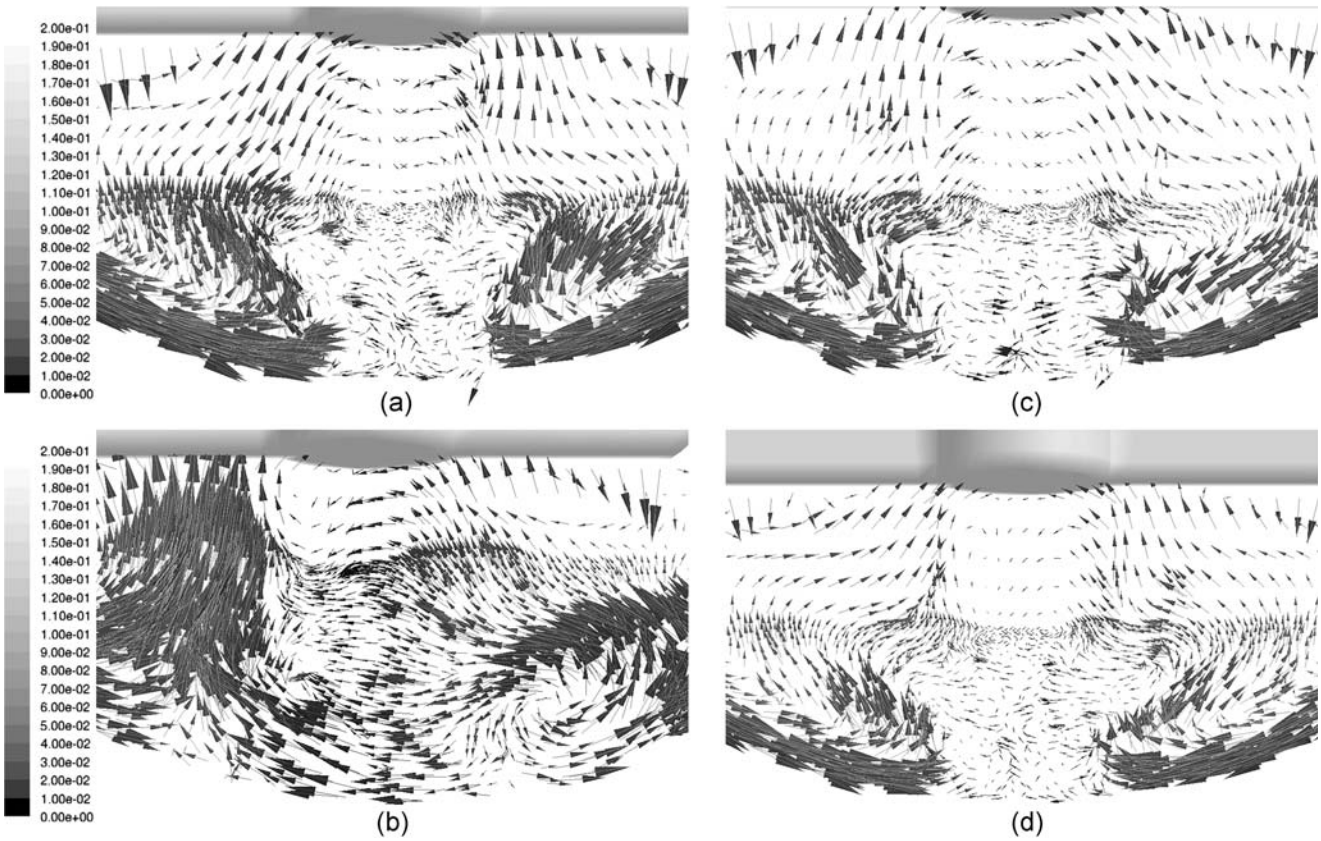

Fig. 9. Numerically predicted velocity vectors (m/s) on the impeller plane (*y*-plane) at the vessel bottom for different locations of the impeller: **a** standard impeller location; **b** off-centered impeller location; **c** higher impeller location; **d** lower impeller location.

was also observed in the lower structured Cooper-type hex mesh domain. In order to produce a smoother strain rate curve in the entire range $-90° < \varphi < 90°$ the CFD-predicted data were interpolated with a 10th order polynomial passing through the predicted value at $\varphi = 0°$ and having a horizontal tangent there. The results are shown in Figs. 14 and 15. Panels (a), (c) and (d) in these figures should be symmetric with respect to the centerline because of the central location of the impeller. The fact that they are not point-by-point symmetric is an artifact of the mesh generator and the solver, which typically produce slightly asymmetric grids to avoid numerical stability problem during numerical iterations. This is especially the case for the fine grid in the bottom region of the vessel.

Three regions can be identified in the strain rate-φ plots in Panels (a), (c), and (d) in Fig. 14. In the first region, extending from 0° to about 10°, and from 0° to about −10°, the strain rate increases linearly from near zero to about 80–100 s^{-1}. In the second region, which goes from about 10° to about 20° and from about −10° to about −20° the strain rates reach a peak value approximately equal to 100–110 s^{-1}. In the third region extending beyond $|\varphi| > 20°$, the strain rate decreases monotonically to about 30 s^{-1} at $|\varphi| = 90°$. A similar picture emerges from the curves on the *x*-plane for the corresponding cases (Panels (a), (c), and (d) in Fig. 15). The strain rate plot for the initial region ($0° < |\varphi| < 10°$) is similar to the *y*-plane case. The peak region is still in the same φ range ($10° < |\varphi| < 20°$), although the peaks are less sharp and more in the shape of a plateau (Fig. 15a and c). In the outer region after the peak, the strain rates decreases monotonically, reaching an even lower value at |φ|=90°. The magnitude of the strain rate was also predicted on the vertical portion of the cylindrical wall and was found to be equal to ~30 s^{-1}, and slowly decreasing with height over a significant portion of the wall of the on the *y*-plane (results not shown). A similar profile was found for the strain rate on the vertical wall in the *x*-plane, although the average value was lower ($\dot{\gamma} \approx 15\ s^{-1}$).

The strain rates profiles were found to be very different for the off-center impeller case (Figs. 14b and 15b). In this case, the strain rate is relatively constant irrespective of φ ($\dot{\gamma} \approx 40 - 50\ s^{-1}$ for the *y*-plane and $\dot{\gamma} \approx 60\ s^{-1}$ for the *x*-plane) and, overall, much smaller than the peak value in the symmetric cases. A small drop for $\dot{\gamma}$ can be see in the central region, for $-10° < \varphi < 10°$. This drop is non-symmetric and more pronounced in the *x*-plane than in the *y*-plane. Overall, the shapes of the strain rate curves for Case (b) are very different from those for the other symmetric cases, even in the central region.

DISCUSSION

The USP Apparatus II is designed to conduct dissolution testing for oral solid dosage forms. Therefore, one of its characteristics should be to provide a homogeneous dissolution environment for the tablet undergoing testing, irrespective of tablet location, in order to generate accurate and reproducible results, especially if the equipment is built and operated according to USP specifications. However, the results of this work, as well as those previously reported by

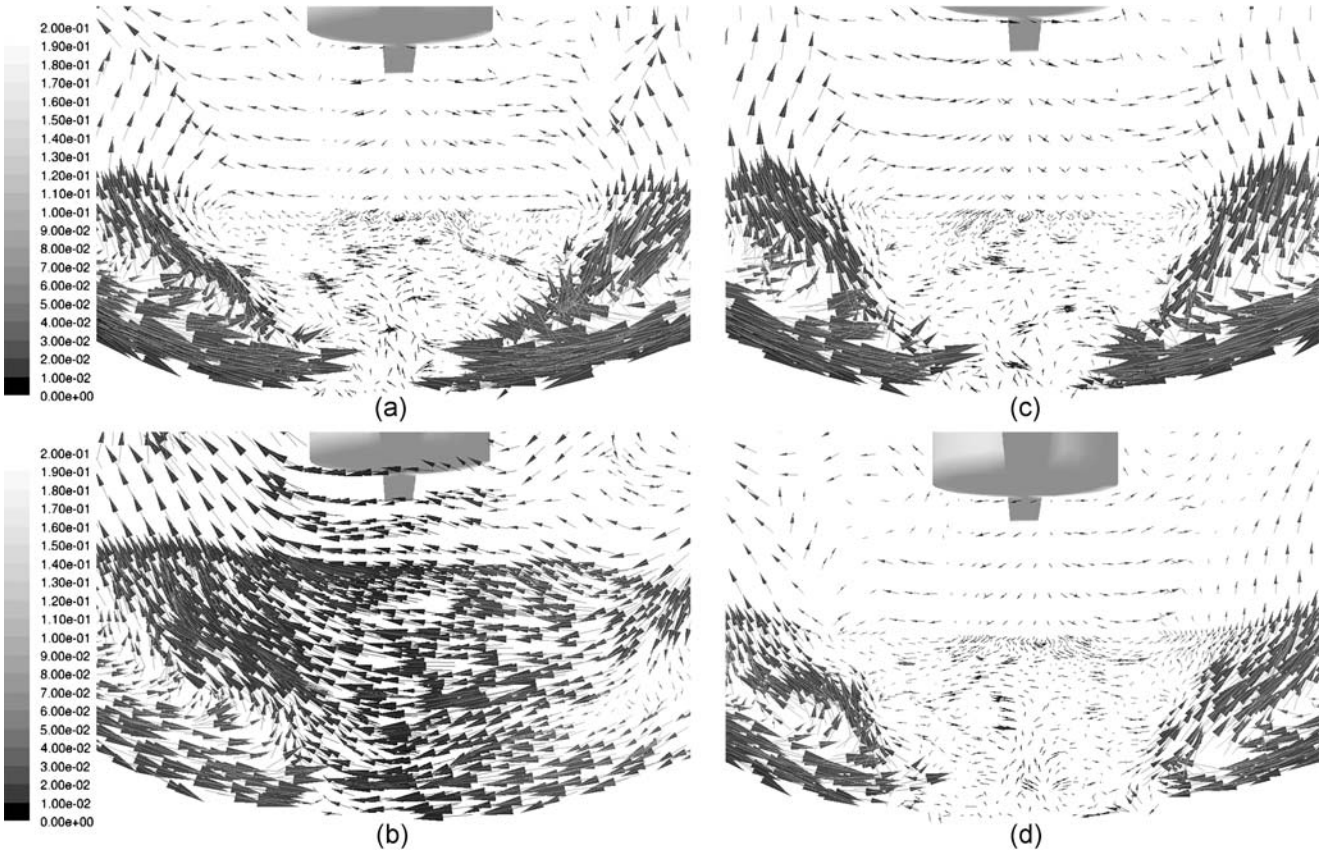

Fig. 10. Numerically predicted velocity vectors (m/s) on the plane perpendicular to the impeller plane (*x*-plane) at the vessel bottom for different locations of the impeller: **a** standard impeller location; **b** off-centered impeller location; **c** higher impeller location; **d** lower impeller location.

this and other groups, clearly show that the velocity distribution in the region just below the impeller is highly non-homogenous, and changes rapidly with position along the vessel bottom, even when the impeller is centrally and symmetrically located within the vessel (19). A similar conclusion can be drawn for the strain rate near the vessel bottom, which is likely to have an even greater impact than the velocity flow field on the tablet–liquid mass transfer, and hence the dissolution rate.

The computational results of the current investigation for the standard impeller location case, previously validated experimentally via LDV (19), are in qualitative agreement with the few previously reported results obtained using quantitative data for the velocity flow field and, especially, strain rates (15,18). Kukura *et al.* (18) and Baxter *et al.* (15) generated CFD-predicted strain rate distribution profiles along the vessel wall of a USP Apparatus II. Their results can be directly compared to those reported here in Fig. 14a, showing similarities but also differences. Both their profiles and our profiles show that the strain rate increases from a very low value in the center of the vessel to a peak in correspondence of $|\varphi| \approx 15° \pm 5°$. However, the results of those authors show that the strain rate has an additional and even higher peak at $|\varphi| \approx 85°$, i.e., very close to the end of the hemispherical section, whereas no such peak appears in our strain rate curves. Instead, our curves show that the strain rate reaches a maximum for $|\varphi| \approx 20°$, and it decreases beyond this value.

Another substantial difference between our strain rate results and those of Kukura *et al.* (18) and Baxter *et al.* (15) is that the strain rate values along the vessel wall are appreciably lower then those found in our work. In their studies, those authors reported that the highest strain rate value for $N = 50$ rpm is less than 10 s^{-1} for $-90° < \varphi < 90°$, whereas in our work the average strain rate values in the same range can be calculated to be between 60 and 70 s^{-1} on both *y*-plane and *x*-plane. The strain rate reported by these investigators for the vertical portion of the cylindrical wall section ($\dot{\gamma} \approx 10 \pm 5\ s^{-1}$) was also lower than that found here ($\dot{\gamma} \approx 30\ s^{-1}$ on the *y*-plane and $\dot{\gamma} \approx 15\ s^{-1}$ on the *x*-plane). These differences could possibly be attributed to the differences in mesh size, CFD solver, discretization method, and turbulence model used. Despite the differences, both our results and the results of Kukura *et al.* (18) and Baxter *et al.* (15) show that the distribution of strain rate on the bottom of the USP Apparatus II is non-uniform and is a strong function of location.

Our results additionally show that the impeller clearance off the vessel bottom, at least within the USP specifications, does not appreciably change the velocity distribution in the bottom portion of the vessel (Fig. 7 and Figs. 9 and 10). More significantly, the strain rate values in the same region, and especially along the bottom vessel wall, do not appear to be significantly affected the impeller clearance (Figs. 12, 13, 14, 15). This is somewhat surprising since one would expect that the distance from the impeller, especially in a region so close

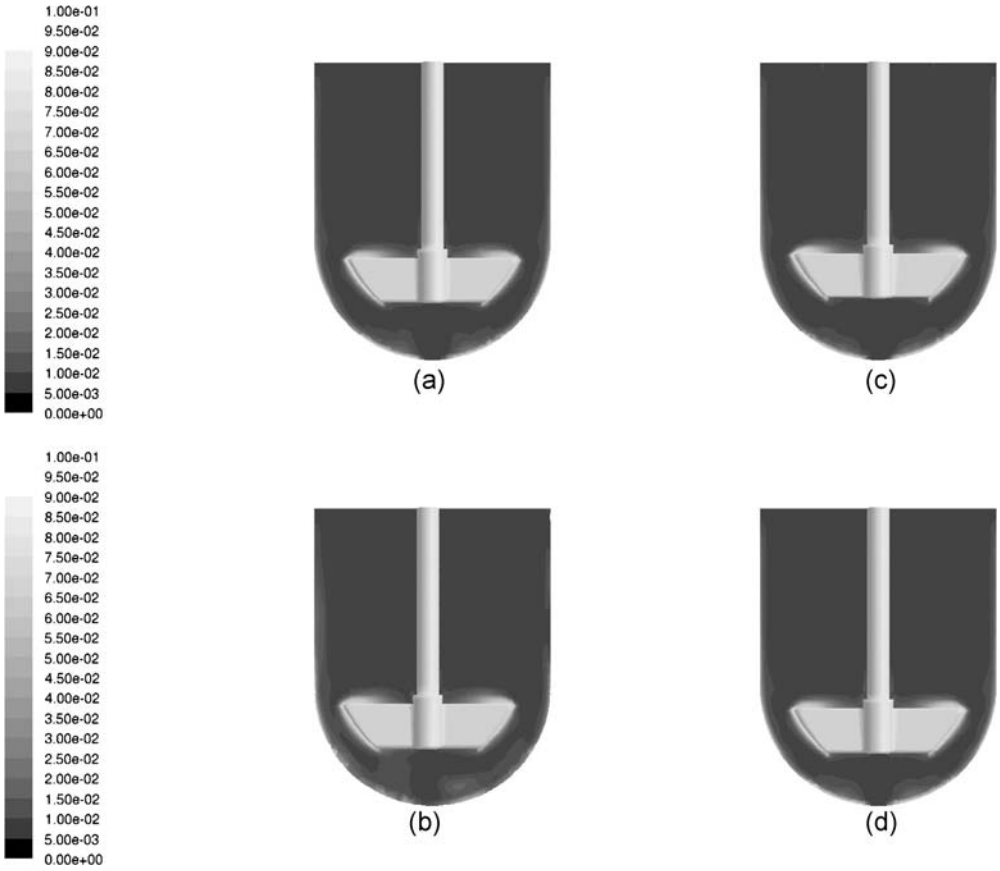

Fig. 11. Numerically predicted contours of the energy dissipation rate (m^2/s^3) on the impeller plane (y-plane) for different locations of the impeller: **a** standard impeller location; **b** off-centered impeller location; **c** higher impeller location; **d** lower impeller location.

to the impeller blades, would play a more dominant role. Instead, it appears that the presence of a low-turbulence, low-shear rate region near the center under the impeller shaft is a key flow pattern characteristic in all cases in which the impeller is centrally located. It should also be stressed that the tangential flow is by far the dominant flow feature in the USP Apparatus II, primarily because of the absence of baffles and the relatively large impeller diameter-to-vessel diameter ratio. Therefore, since varying the impeller clearance does not alter the system's symmetry, the predominance of the tangential velocity on the overall flow remains nearly unchanged, especially if the impeller clearance varies only within ±8% of the standard value, as in this case. However, small changes can be observed in the axial and radial velocity components and in the strain rates as a result of impeller clearance. In general, the impact of impeller clearance on less critical features of flow pattern is typically complex and difficult to predict from first principles, and non-linear effects on flow-dependent phenomena caused by variation in impeller clearance have been reported in the past. For example, Armenante and Uehara Nagamine (25) studied the effect of impeller clearance on solid suspension and power dissipation in liquids stirred in mechanically agitated, baffled, cylindrical vessels. They observed that, depending on the impeller type, the minimum impeller speed, N_{js}, to achieve complete off-bottom suspension for finely dispersed solids could change in a non-monotonic fashion, i.e., that decreasing the impeller clearance typically produced a reduction in N_{js}, but that further reduction in clearance when the impeller was already close to the vessel bottom actually resulted in a small but noticeable *increase* in N_{js}. Their explanation was that a "choking" effect occurs when the impeller is placed very close to the vessel bottom, forcing the fluid pumped by the impeller to rapidly change direction in a very small zone (because of the reduced gap between the impeller blades and the vessel bottom), thus resulting in increased energy dissipation, and hence a greater power consumption by the impeller, and reduced pumping effectiveness, and hence greater N_{js}. Although in their case the presence of baffles and the different impeller and vessel geometries generated a flow pattern quite dissimilar from that observed in the USP Apparatus II, this example shows that impeller-vessel interactions can be quite strong and generate somewhat unexpected results. In the case of the USP Apparatus II, two counteracting effects are at work when the impeller clearance is changed. When the impeller is raised, the off-bottom impeller clearance increases, thus weakening the influence of the impeller on the flow below it. However, raising the impeller also increases the gap between the blade tip and the vertical-hemispherical vessel wall, thus promoting a stronger radial flow in the gap, which in turn results in a stronger downward flow in the region below the impeller. When the impeller is lowered, the reverse is true: the reduced off-bottom clearance strengthens the influence of the impeller on the flow below it, but reduces the blade tip-vessel wall gap, thus partially "choking" the radial

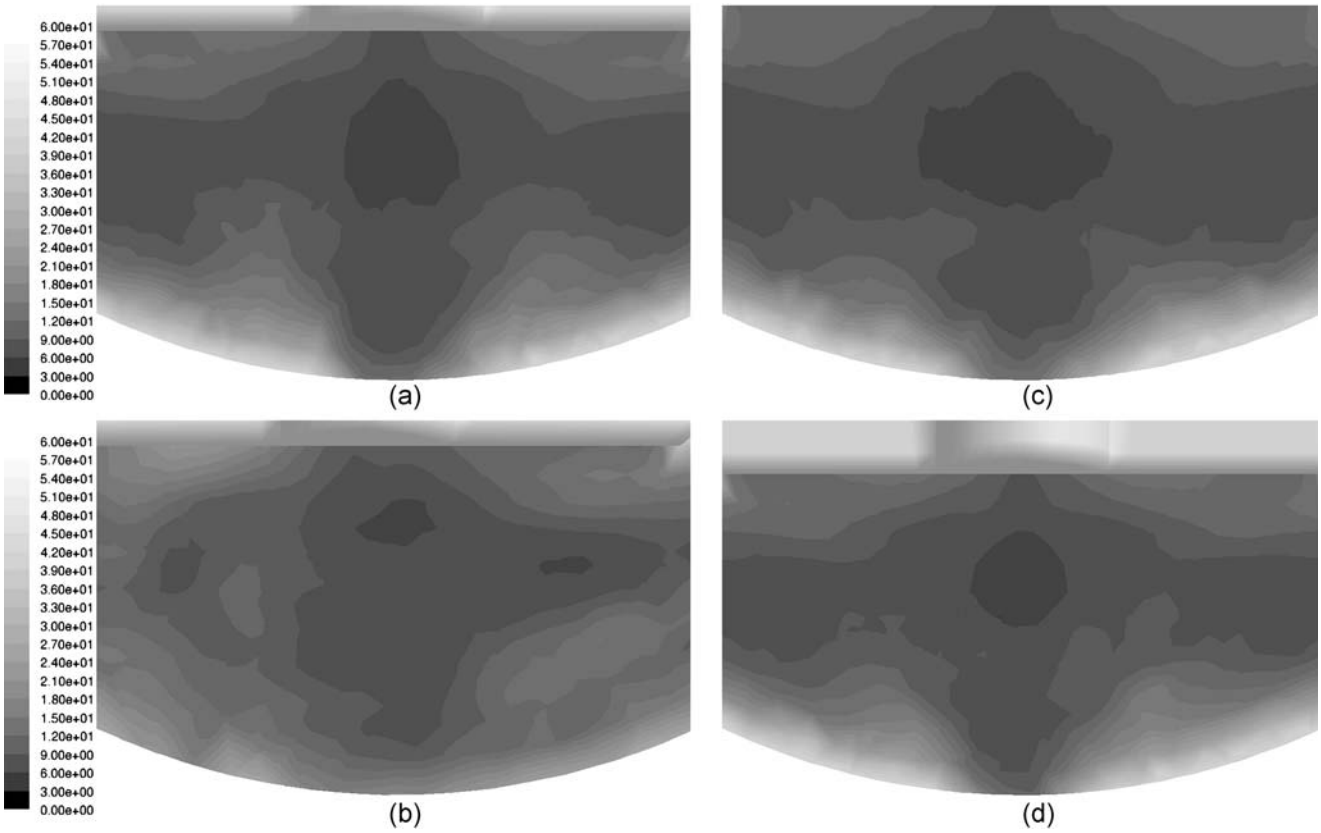

Fig. 12. Numerically predicted contours of the strain rate (1/s) on the impeller plane (*y*-plane) at the vessel bottom for different locations of the impeller: **a** standard impeller location; **b** off-centered impeller location; **c** higher impeller location; **d** lower impeller location.

flow in the gap and reducing the intensity of the jet that penetrates the lower vessel region. The likely overall result is that these effects partially offset each other, and that the impeller clearance ends up having a limited impact on the flow below the impeller, at least for the case in which the variations in impeller clearance are relatively small, as in our case.

However, the results of the present study clearly show that the velocity distribution and the strain rate distribution are strongly affected by the off-center placement of the impeller, even when such a displacement is only 2 mm, as allowed under USP specifications (Panels (b) in Figs. 5, 6, 7, 8, 9, 10, 11, 12, 13, 14, 15). Even for the off-center case, the flow is dominated by the tangential component of the velocity (Fig. 7b), as in all unbaffled stirred vessels. However, the loss of symmetry resulting from the off placement of the impeller partially disrupts the rotational flow associated with a centrally located impeller, resulting in stronger axial and radial flows in the region below the impeller (Figs. 9b and 10b). The velocity changes also affect the magnitude and distribution of the strain rate near the vessel bottom, which become much more uniformly distributed than in all the cases in which the impeller is centrally located (Figs. 14 and 15).

It should be stressed, again, that the results presented here were obtained with only a 5% lateral translation of the impeller. Although our results were obtained with the largest off-center impeller placement allowed by the USP (2 mm), one could speculate that smaller off-center impeller locations could also have similar effects, although not of equal intensity. It is therefore conceivable that some of the variability and, possibly, even failures, associated with dissolution testing and reported in the literature (11–13) could be attributed to the off-center location of the impeller, especially if this effect is combined with other geometric effects, such as an off-center resting location of the tablet resulting from the randomness of the tablet vertical trajectory while sinking after its introduction in the vessel at the beginning of the test. Loss of central impeller symmetry could be the result of a number of factors, especially in older equipment, such as operator's error, worn couplings, misplacement of the vessel, or a bent shaft.

Given the absence of baffles, the flow and shear rate in the USP Apparatus II are expected to be highly sensitive to any geometric factors that may affect its symmetry (or lack thereof). This is one of the reasons why equipment manufacturers have tried over the years to reduce any mechanical defects that could result in loss of symmetry, e.g., by introducing self-centering shafts, certified vessels, and tools to determine vessel eccentricity. Interestingly, one could propose that a possible method to reduce variability during the test would be precisely the opposite, i.e., to deliberately introduce non-symmetry in the system, e.g., through the off-center placement of the impeller, which would result in a more uniform shear rate near the vessel bottom where the tablet is located.

Further studies need to be conducted in order to find out quantitatively how the non-uniform distribution of strain rate can affect the dissolution rates.

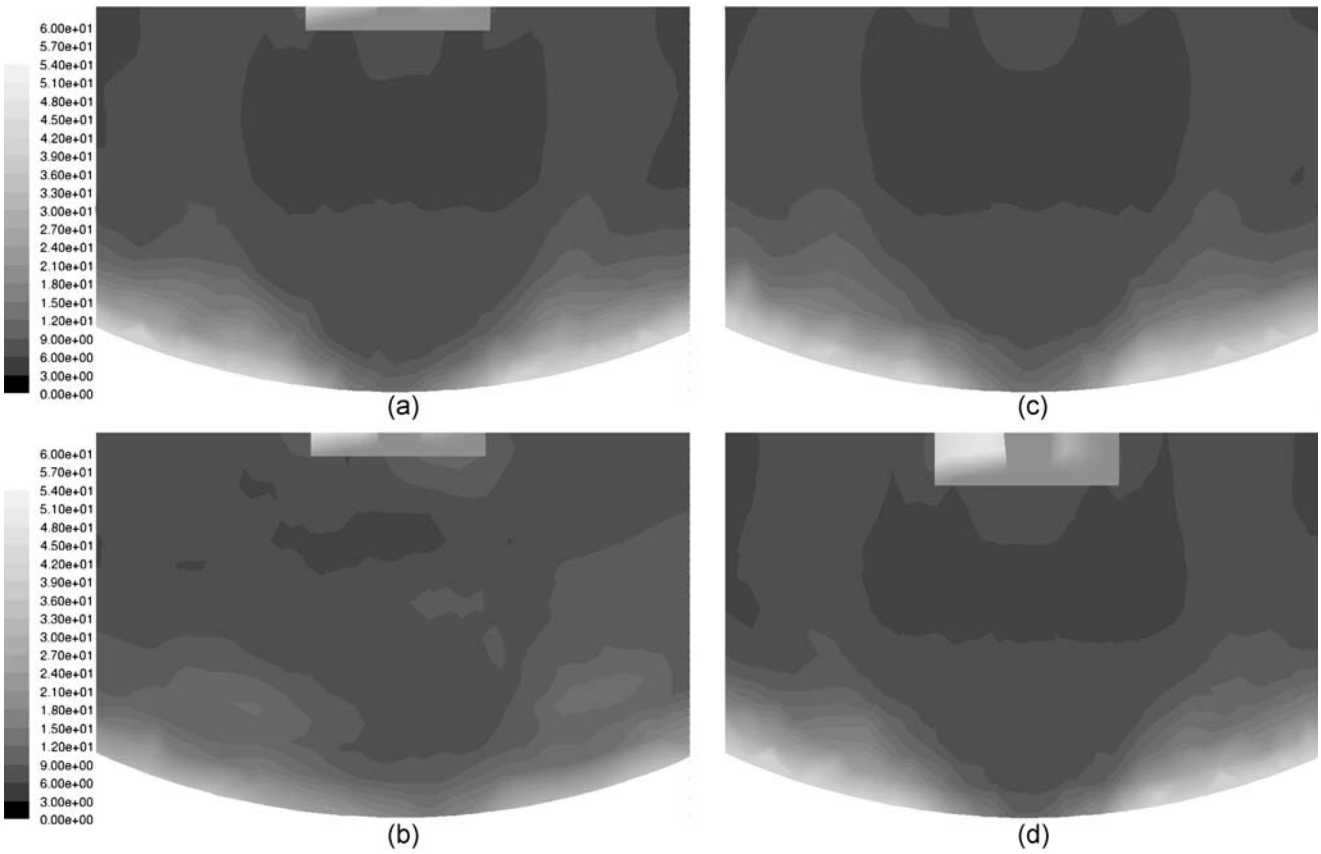

Fig. 13. Numerically predicted contours of the strain rate (1/s) on the plane perpendicular to the impeller plane (x-plane) at the vessel bottom for different locations of the impeller: **a** standard impeller location; **b** off-centered impeller location; **c** higher impeller location; **d** lower impeller location.

CONCLUSIONS

A number of conclusions can be drawn from this work:

1. The flow inside the USP Apparatus II is dominated by the tangential component of the velocity, irrespective of the location of the impeller in the vessel examined in this work.
2. For all the cases in which the impeller is centrally located (standard impeller clearance, 2 mm higher impeller, and 2 mm lower impeller) the axial and radial components of the velocity are symmetrically distributed with respect to the vessel centerline and are very weak in the region below the impeller, especially in the region under the shaft. When the impeller is placed 2 mm off center the symmetrical structure and the poorly mixed region below the shaft observed in the standard case are largely removed, thus promoting better mixing and recirculation in the lower vessel region where the tablet resides.
3. Irrespective of the impeller clearance, when the impeller is centrally located, the strain rate distribution along the vessel bottom is highly non-uniform. In this case, the shear rate is very weak below the shaft, but increases rapidly to reach a peak value some 15°–20° away from the centerline. In the outer region on the vessel bottom the shear rate then declines with distance from the centerline. When the impeller is placed 2 mm off center the strain rate distribution is significantly more uniform almost everywhere along the vessel bottom wall.
4. It appears that varying the impeller off bottom clearance within the limits specified in the USP (25 ± 2 mm) has little impact on the flow pattern, velocity magnitudes, and strain rate distribution near the vessel bottom. However, placing the impeller off center even within the limits specified in the USP (2 mm) can have significant effects on the flow field, velocity magnitude, and strain rate near the vessel bottom. This, in turn, is likely to significantly affect the liquid–tablet mass transfer rate and hence the rate of dissolution.
5. Given the extreme sensitivity of the USP Apparatus II to loss of symmetry, it is conceivable that smaller off-center impeller displacements, such as those introduced by operator's error, equipment wear, and improper impeller misalignment, could also lead to appreciable variations in the fluid flow and strain rate, potentially introducing variability in the test results.

ACKNOWLEDGEMENT

This work was partially supported through a grant from Merck & Co., West Point, PA, whose contribution is gratefully acknowledged. The authors also wish to thank Drs. Russell Plank, Michael Gentzler, Kenneth Ford, Paul Harmon and Scott Reynolds for their contribution and support.

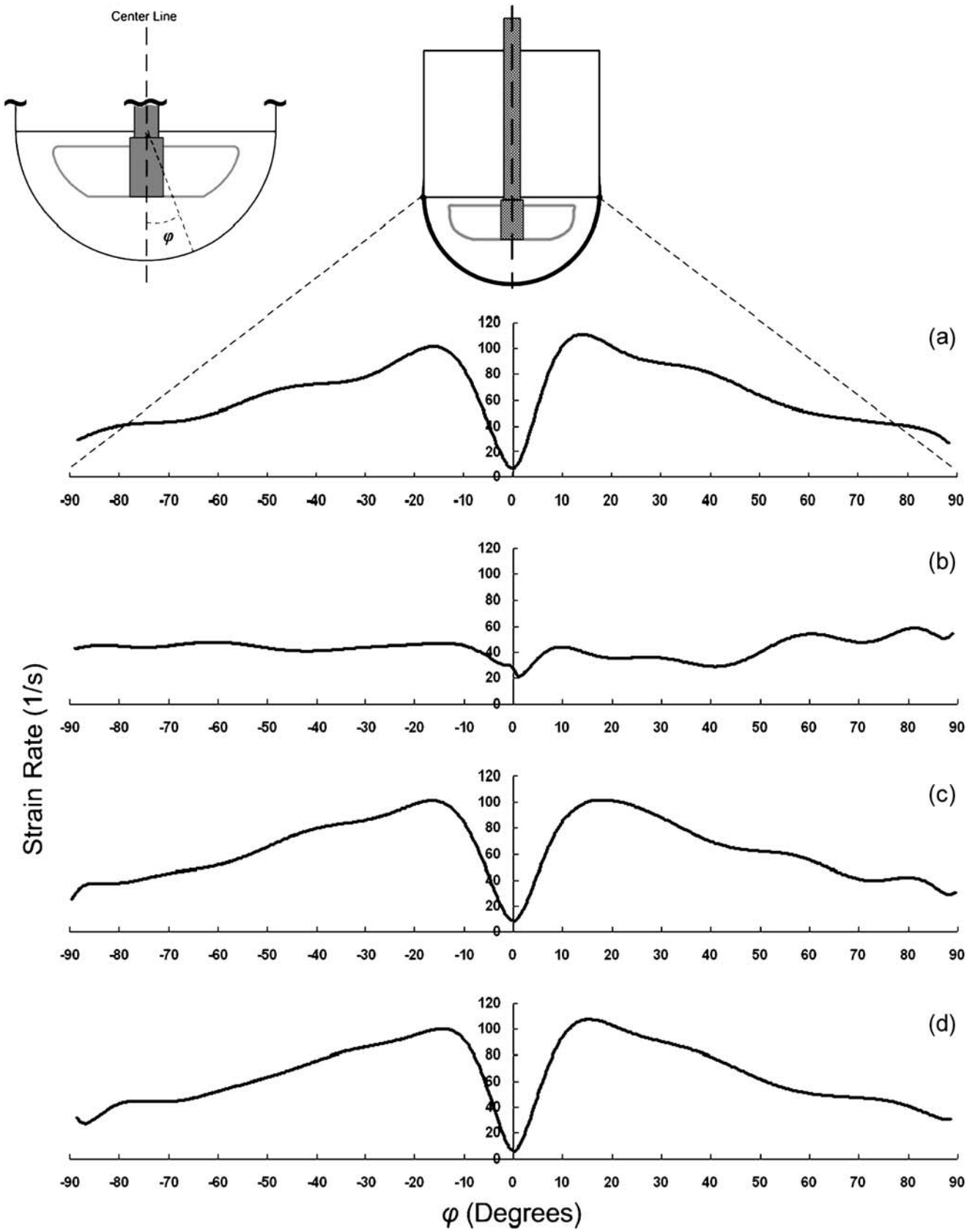

Fig. 14. Numerically predicted strain rate (1/s) along the bottom of the vessel wall on the impeller plane (*y*-plane) as a function of angular position from centerline for different locations of the impeller: **a** standard impeller location; **b** off-centered impeller location; **c** higher impeller location; **d** lower impeller location.

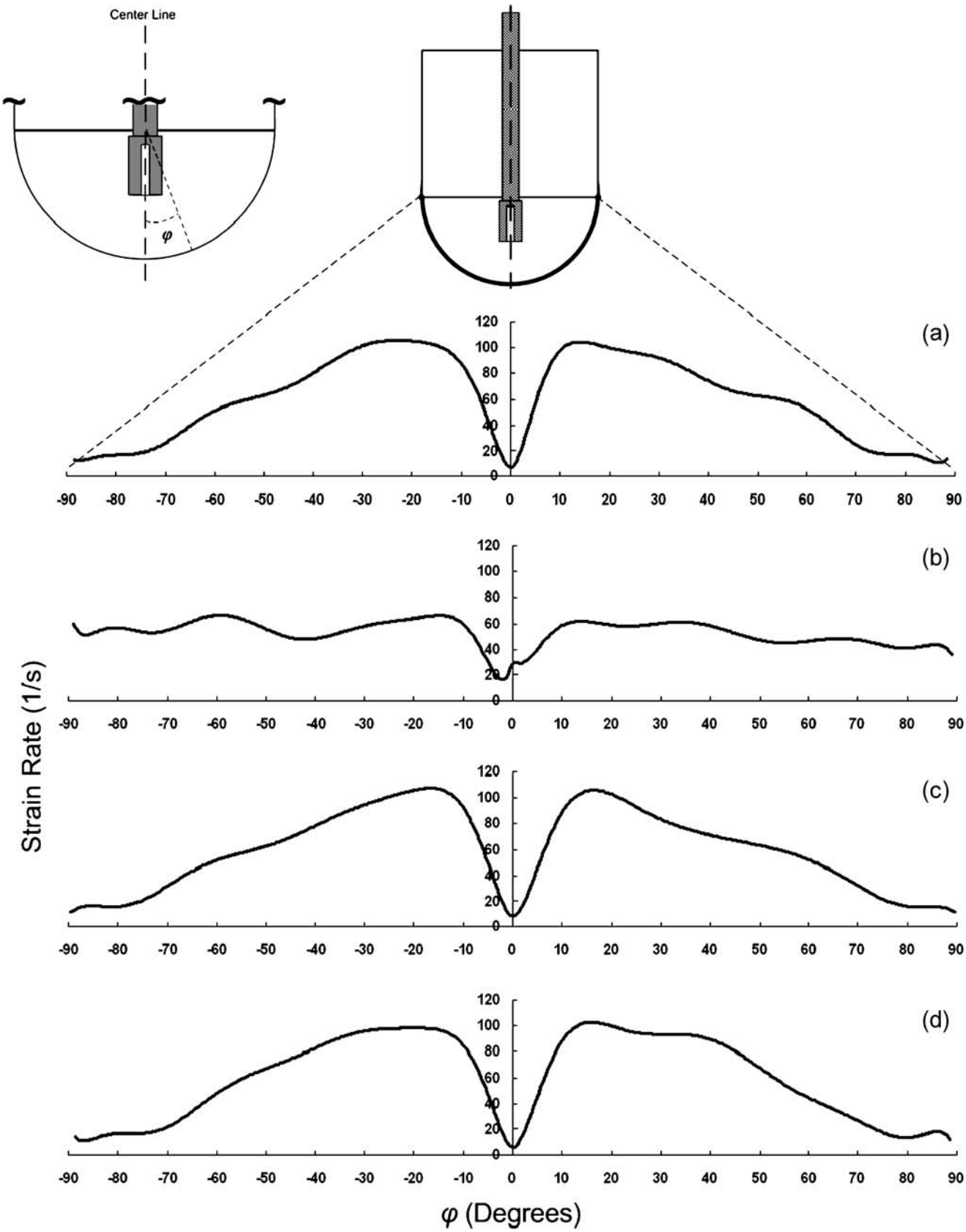

Fig. 15. Numerically predicted strain rate (1/s) along the bottom of the vessel wall on the plane perpendicular to the impeller plane (*x*-plane) as a function of angular position from centerline for different locations of the impeller: **a** standard impeller location; **b** off-centered impeller location; **c** higher impeller location; **d** lower impeller location.

REFERENCES

1. The United States Pharmacopeia & The National Formulary. The Official Compendia of Standards, USP 29-NF 24 2005, US Pharmacopeial Convention Inc., November 2005.
2. J. L. Cohen, B. B. Hubert, L. J. Leeson, C. T. Rhodes, J. R. Robinson, T. J. Roseman, and E. Shefter. The development of USP dissolution and drug release standards. *Pharm. Res.* **7**:983–987 (1990).
3. J. Mauger, J. Ballard, R. Brockson, S. De, V. Gray, and D. Robinson. Intrinsic dissolution performance of the USP dissolution apparatus 2 (rotating paddle) using modified salicylic acid calibration tablets: proof of principle. *Dissol. Technol.* **10**(3):6–15 (2003).
4. T. W. Moore, J. F. Hamilton, and C. M. Kerner. Dissolution testing: limitation of USP prednisone and salicylic acid calibrator tablets. *Pharmacopeial Forum* **21**:1387–1396 (1995).
5. S. A. Qureshi, and I. J. McGilveray. Typical variability in drug dissolution testing: study with USP and FDA calibrator tablets and a marketed drug (Glibenclamide) product. *Europ. J. Pharm. Sci.* **7**:249–258 (1999).
6. S. A. Qureshi, and J. Shabnam. Cause of high variability in drug dissolution testing and its impact on setting tolerances. *Europ. J. Pharm. Sci.* **12**:271–276 (2001).
7. P. Costa, and J. M. S. Lobo. Influence of dissolution medium agitation on release profiles of sustained-release tablets. *Drug Devel. Ind. Pharm.* **27**:811–817 (2001).
8. L. M. Bocanegra, G. J. Morris, J. T. Jurewicz, and J. W. Mauger. Fluid and particle laser doppler velocity measurements and mass transfer predictions for USP paddle method dissolution apparatus. *Drug Devel. Ind. Pharm.* **16**:1441–1464 (1990).
9. D. C. Cox, and W. B. Furman. Systematic error associated with Apparatus 2 of the USP dissolution test. I. Effects of physical alignment of the dissolution apparatus. *J. Pharm. Sci.* **71**:451–452 (1982).
10. D. C. Cox, W. B. Furman, L. K. Thornton, T. W. Moore, and E. H. Jefferson. Systematic error associated with apparatus 2 of the USP dissolution test. III. Limitations of calibrators and the USP suitability test. *J. Pharm. Sci* **72**:910–913 (1983).
11. FDC Reports. Recalls Prompted By FDA on the Increase. *The Gold Sheet* 35 (1) (2001).
12. FDC Reports. Counterfeits Pose Special Recall Challenge. *The Gold Sheet* 36 (1) (2002).
13. FDC Reports. Spike in Potency-Related Problems Contributes to Overall Rise in 2002 Recalls. *The Gold Sheet* 37 (1) (2003).
14. J. Kukura, P. C. Arratia, E. S. Szalai, and F. J. Muzzio. Engineering tools for understanding hydrodynamics of dissolution tests. *Drug Devel. Ind. Pharm.* **29**:231–239 (2003).
15. J. L. Baxter, J. Kukura, and F. J. Muzzio. Hydrodynamics-induced variability in the USP apparatus II dissolution Test. *Int. J. Pharmaceutics* **292**:17–28 (2005).
16. L. McCarthy, G. Bradley, J. Sexton, O. Corrigan, and A. M. Healy. Computational fluid dynamics modeling of the paddle dissolution apparatus: agitation rate mixing patterns and fluid velocities. *AAPS Pharm. Sci. Tech.* **5**(2) Article 31 (2004).
17. L. McCarthy, C. Kosiol, A. M. Healy, G. Bradley, J. Sexton, and O. Corrigan. Simulating the hydrodynamic conditions in the United States Pharmacopeias paddle dissolution apparatus. AAPS *Pharm. Sci. Tech.* **4**(2) Article 22 (2003).
18. J. Kukura, J. L. Baxter, and F. J. Muzzio. Shear distribution and variability in the USP Apparatus 2 under turbulent conditions. *Int. J. Pharmaceutics* **279**:9–17 (2004).
19. G. Bai, P. M. Armenante, R. V. Plank, M. Gentzler, K. Ford, and P. Harmon. Hydrodynamic investigation of USP dissolution test apparatus II. *J. Pharm. Sci* **96**(9):2327–2349 (2007).
20. G. Bai, P. M. Armenante, and R. V. Plank. Experimental and computational determination of blend time in USP dissolution testing apparatus II. *J. Pharm. Sci* **96**(11):3072–3086 (2007).
21. Fluent 6.2 User's Guide. Fluent Inc. New Hampshire (2005).
22. P. M. Armenante, and D. J. Kirwan. Mass transfer to microparticles in agitated systems. *Chem. Eng. Sci.* **44**:2781–2796 (1989).
23. D. M. Levins, and J. R. Glastonbury. Application of Kolmogoroff's theory to particle–liquid mass transfer in agitated vessels. *Chem. Eng. Sci.* **27**(3):537–543 (1972).
24. R. B. Bird, E. W. Stewart, and N. F. Lightfoot. *Transport Phenomena*. Wiley, New York, 2002.
25. P. M. Armenante, and E. Uehara Nagamine. Effect of low off-bottom impeller clearance on the minimum agitation speed for complete suspension of solids in stirred tanks. *Chem. Eng. Sci.* **53**:1757–1775 (1998).